Mechanics of Internal Waves Propagating over a Varying Bottom Slope

Motohiko Umeyama[3]

Abstract: We studied theoretically and experimentally the transformation, attenuation, and setup due to shoaling and breaking of internal waves in a two-layer fluid system on a uniform slope. An image processing technique was used to illustrate 2D instantaneous displacements of density interface. These results were compared with the calculated values by using the method of characteristics, the simple shoaling model with energy dissipation, and the momentum balance equation based on a radiation stress concept. We also measured the upper and lower velocity fields for progressive internal waves by using Particle Image Velocimetry (PIV).

Keywords: Internal waves; Slopes; Setup; Radiation stress; Image processing technique; PIV

1. Introduction

The mechanism of internal waves in a two-layer system comprising homogeneous fluids of slightly different densities has been studied in the Coastal and Ocean Engineering Laboratory at Tokyo Metropolitan University. In the research of Umeyama (2002), an image processing technique was first used to illustrate the temporal variations of the density interface in a wave tank. Umeyama and Shintani (2004) installed a Plexiglas plate in the same wave tank, to observe the runup and breaking of internal waves over it. The profile of internal waves and the mixture of upper and lower layer waters were obtained using more advanced imaging technique. Later, Umeyama and Shintani (2006) extended the aspects of internal wave mechanics into the transformation, attenuation, setup, and undertow during shoaling and breaking events. Experiments were performed over a gentle slope, and the observed data were used to confirm theoretical solutions by the method of characteristics, the energy dissipation model with the radiation stress, and the momentum balance equation. Recently, Umeyama (2008) studied transformation processes and nonlinear properties of internal waves over a uniform slope in a two fluid system, attempting to reveal water particle kinematics by using Particle Image Velocimetry (PIV). The scope of the investigation extends into the physics for partial standing internal waves.

Although much research has been devoted to experimentally investigating the mechanism of the breaking and mixing of internal waves propagating on a uniform slope, the peculiar features of the wave-induced flows are still not understood. The objective of this study is to review the dynamics and kinematics of internal waves during a runup event using a video recording system and a new PIV system.

2. Internal Wave Theories

2.1 Basic Internal Wave Solution

We consider internal waves propagating along the interface between two homogeneous incompressible and inviscid fluids of different density. The origin of the axes is located in

[3] Department of Civil and Environmental Engineering, Tokyo Metropolitan University, Japan;
E-mail: umeyama-motohiko@c.metro-u.ac.jp

the undisturbed interface. The density and depth of the upper layer are ρ_{I} and h_{I}, and those of the lower layer are ρ_{II} and h_{II}. The vertical displacements of the free surface and the density interface are $\eta_{\mathrm{I}}(x,t)$ and $\eta_{\mathrm{II}}(x,t)$. Let $\varphi_{\mathrm{I}}(x,z,t)$, and $\varphi_{\mathrm{II}}(x,z,t)$ denote the velocity potentials in the upper and lower layers, so that the Laplace equations are

$$\varphi_{\mathrm{Ixx}} + \varphi_{\mathrm{Izz}} = 0 \tag{1}$$

$$\varphi_{\mathrm{IIxx}} + \varphi_{\mathrm{IIzz}} = 0 \tag{2}$$

where x = horizontal coordinate; and z = vertical coordinate. The kinematical and dynamical boundary conditions at the free surface are

$$g\left(\eta_I + h_I\right) + \phi_{It} + \frac{1}{2}\left(\phi_{Ix}^2 + \phi_{Iz}^2\right) = 0 \qquad \text{on } z = h_{\mathrm{I}} + \eta_{\mathrm{I}} \tag{3}$$

$$\eta_{It} + \eta_{Ix}\phi_{Ix} - \phi_{Iz} = 0 \qquad \text{on } z = h_{\mathrm{I}} + \eta_{\mathrm{I}} \tag{4}$$

where g = gravity acceleration; and t = time. The boundary conditions at the density interface are

$$\eta_{IIt} + \eta_{IIx}\phi_{Ix} - \phi_{Iz} = 0 \qquad \text{on } z = \eta_{\mathrm{II}} \tag{5}$$

$$\eta_{IIt} + \eta_{IIx}\phi_{IIx} - \phi_{IIz} = 0 \qquad \text{on } z = \eta_{\mathrm{II}} \tag{6}$$

$$\rho_I\left\{g\eta_{II} + \phi_{It} + \frac{1}{2}\left(\phi_{Ix}^2 + \phi_{Iz}^2\right)\right\} = \rho_{II}\left\{g\eta_{II} + \phi_{IIt} + \frac{1}{2}\left(\phi_{IIx}^2 + \phi_{IIz}^2\right)\right\} \qquad \text{on } z = h_{\mathrm{I}} + \eta_{\mathrm{I}} \tag{7}$$

The bottom boundary condition is

$$\phi_{IIz} = 0 \qquad \text{on } z = -h_{\mathrm{II}} \tag{8}$$

In the finite-amplitude wave theory, the perturbation method is used to solve the above basic equations and boundary conditions. The velocity potentials, vertical displacements of free surface and density interface, and angular frequency for an nth-order wave of finite amplitude can be expressed as

$$\phi_I = \varepsilon\phi_I^{(1)} + \varepsilon^2\phi_I^{(2)} + \varepsilon^3\phi_I^{(3)} + \ldots + \varepsilon^n\phi_I^{(n)} + O\left(\varepsilon^{n+1}\right)$$

$$\phi_{II} = \varepsilon\phi_{II}^{(1)} + \varepsilon^2\phi_{II}^{(2)} + \varepsilon^3\phi_{II}^{(3)} + \ldots + \varepsilon^n\phi_{II}^{(n)} + O\left(\varepsilon^{n+1}\right)$$

$$\eta_I = \varepsilon\eta_I^{(1)} + \varepsilon^2\eta_I^{(2)} + \varepsilon^3\eta_I^{(3)} + \ldots + \varepsilon^n\eta_I^{(n)} + O\left(\varepsilon^{n+1}\right)$$

$$\eta_{II} = \varepsilon\eta_{II}^{(1)} + \varepsilon^2\eta_{II}^{(2)} + \varepsilon^3\eta_{II}^{(3)} + \ldots + \varepsilon^n\eta_{II}^{(n)} + O\left(\varepsilon^{n+1}\right)$$

$$\sigma = \sigma^{(0)} + \varepsilon\sigma^{(1)} + \varepsilon^2\sigma^{(2)} + \ldots + \varepsilon^{n-1}\sigma^{(n-1)} + O\left(\varepsilon^n\right)$$

where ε = perturbation parameter; σ = angular frequency; and $O(\ )$ = order symbol. The superscript (n) denotes a quantity corresponding to the nth-order perturbation solution. These solutions have been obtained to the second order by Umeyama (1998), and to the third order by Umeyama (2002).

When the displacement of fluid interface is given by $\eta_{\mathrm{II}}(x,t) = a\cos(kx-\sigma t)$, the horizontal and vertical velocity components for the water particle can be obtained from the velocity potentials where $u_{\mathrm{I}} = -\partial\varphi_{\mathrm{I}}/\partial\mathrm{x}$, $w_{\mathrm{I}} = -\partial\varphi_{\mathrm{I}}/\partial\mathrm{z}$, $u_{\mathrm{II}} = -\partial\varphi_{\mathrm{II}}/\partial\mathrm{x}$, and $w_{\mathrm{II}} = -\partial\varphi_{\mathrm{II}}/\partial\mathrm{z}$. Therefore, the velocity components in both layers are expressed as

$$u_I = \frac{ak}{\sigma}\left(\alpha\cosh kz - \frac{\sigma^2}{k}\sinh kz\right)\cos\left(kx-\sigma t\right) \tag{9}$$

$$w_I = -\frac{ak}{\sigma}\left(\alpha\sinh kz - \frac{\sigma^2}{k}\cosh kz\right)\sin\left(kx-\sigma t\right) \tag{10}$$

$$u_{II} = -\frac{a\sigma}{\sinh kh_{II}}\cosh k\left(z+h_{II}\right)\cos\left(kx-\sigma t\right) \tag{11}$$

$$w_{II} = \frac{a\sigma}{\sinh kh_{II}}\sinh k\left(z+h_{II}\right)\sin\left(kx-\sigma t\right) \tag{12}$$

where a = amplitude of internal waves; k = wave number; and α = constant that is given by

$$\alpha = \frac{\rho_{II}-\rho_I}{\rho_I}g - \frac{\rho_{II}}{\rho_I}\frac{\sigma^2}{k}\coth kh_{II}$$

The dispersion relation may be written as

$$\sigma^4\left(\coth kh_I\coth kh_{II} + \frac{\rho_I}{\rho_{II}}\right) - \sigma^2\left(\coth kh_I + \coth kh_{II}\right)gk + \frac{\rho_{II}-\rho_I}{\rho_{II}}\left(gk\right)^2 = 0 \tag{13}$$

Solving Eq.(13) for $C = \sigma/k$ and assuming $\rho_{II} \approx \rho_I$, it becomes

$$C = \sqrt{\frac{\rho_{II}-\rho_I}{\rho_{II}}\frac{g}{k\left(\coth kh_I + \coth kh_{II}\right)}} \tag{14}$$

Thus the group velocity for internal waves is given by

$$C_g = \frac{C}{2}\left(1+\frac{\dfrac{kh_I}{\sinh^2 kh_I}+\dfrac{kh_{II}}{\sinh^2 kh_{II}}}{\coth kh_I+\coth kh_{II}}\right) \tag{15}$$

2.2 Method of Characteristics for Long Internal Waves on a Slope

Umeyama and Shintani (2004) investigated the runup of internal waves on a plane impermeable slope. A reliable solution for the displacement of the density interface and the horizontal velocity of the internal waves was derived by means of the method of characteristics. Let $u_{II}(x,z,t)$ denotes the horizontal velocity for long internal waves so that the governing equations are

$$2\left(1+\frac{\eta_{II}+h_{II}}{h_I}\right)C_t + u_{IIx}C + 2\left(1+\frac{\eta_{II}+h_{II}}{h_I}\right)C_x = 0 \tag{16}$$

$$u_{IIt} + u_{II}u_{IIx} + 2\left(1+\frac{\eta_{II}+h_{II}}{h_I}\right)^2 CC_x = g\frac{\rho_{II}-\rho_I}{\rho_{II}}h_{IIx} \tag{17}$$

It is convenient to define the lower-layer thickness for a uniform slope as

$$h_{II} = h_{II}(x) = m\frac{\rho_{II}}{g(\rho_{II}-\rho_I)}x$$

where m is a constant. By adding and subtracting Eqs.(16) and (17), and assuming $\eta + h_{II} << h_I$, the results can be written in the familiar form:

$$[\frac{\partial}{\partial t} + (u_{II} \pm C)\frac{\partial}{\partial x}](u_{II} \pm C - mt) = 0 \tag{18}$$

Use of the method of characteristics will make it possible to describe η_{II} and u_{II} such as

$$\eta_{II} = -\frac{A^2}{2}\frac{h_I + sx}{h_I sx}[J_1(X)\cos(T) + \{J_0(X) - \frac{s}{2\sigma}\frac{J_1(X)}{X}\}\sin(T)]^2 + A\{J_0(X)\sin(T) + J_1(X)\cos(T)\} \tag{19}$$

$$u_{II} = \frac{A}{X}[J_1(X)\cos(T) + \{J_0(X) - \frac{s}{2\sigma}\frac{J_1(X)}{X}\}\sin(T)] \tag{20}$$

where A = constant, and J_p = the Bessel function of order p, and

$$X = \sqrt{(\frac{h_I sx}{h_I + sx}) \Big/ (\frac{\rho_{II} - \rho_I}{\rho_{II}} g)} \text{ and } T = -\sigma t$$

2.3 Radiation Stress, Setup, and Attenuation for Internal Waves

During the passage of surface waves, there are mean transport of water upward the shoreline and depression of the mean water level from the still water level. Longuet-Higgins and Stewart (1964) introduced the radiation concept to prove these mechanisms, and Umeyama (2006) applied it to internal waves. The principal component of the radiation stress for internal waves can be defined as

$$S_{xx} = \overline{\int_{\eta_{II}}^{\eta_I + h_I} (p_I + \rho_I u_I^2)dz} - \int_0^{h_I} p_{I0}dz + \overline{\int_{-h_{II}}^{\eta_{II}} (p_{II} + \rho_{II} u_{II}^2)dz} + \int_{-h_{II}}^{0} p_{II0}dz \tag{21}$$

where S_{xx} = radiation stress for internal waves; p_{I0} = hydrostatic pressure in the upper layer; p_{II0} = hydrostatic pressure in the lower layer; and the over-bar denotes averaging in time over a wave period. Assuming that the upper limit of integration may be replaced by $z = h_I$, the displacement of the density interface is small relative to the wavelength, and the mean mass flux of vertical momentum across a horizontal plane balances with the weight of the water above it, Eq.(21) reduces to

$$S_{xx} = \int_0^{h_I} \rho_I \overline{(u_I^2 - w_I^2)}dz + \int_{-h_{II}}^{0} \rho_{II} \overline{(u_{II}^2 - w_{II}^2)}dz \tag{22}$$

Substituting Eqs.(9)-(12) into Eq.(22), the radiation stress of internal waves becomes

$$S_{xx} = \frac{a^2}{2}\{\rho_I(\frac{k^2 h_I}{\sigma^2}\alpha^2 - \sigma^2 h_I) + \frac{\rho_{II}\sigma^2 h_{II}}{\sinh^2 kh_{II}}\} \tag{23}$$

The changes in radiation stress lead to changes in the mean level of the fluid interface when internal waves encounter a sloping beach. The equilibrium between radiation stress change and average slope of the fluid interface yields

$$\frac{dS_{xx}}{dx} - \{\rho_I - \rho_{II}\}g(\overline{\eta} + h_{II})\frac{d\overline{\eta}}{dx} = 0 \tag{24}$$

Generally, the attenuation of internal waves in the continental slope is a complicated hydrodynamic process. For the purpose of the present study it may be helpful to use a model in which the divergence of the energy flux is balanced by the dissipation. Therefore, the equation of energy conservation can be expressed as

$$\frac{dF}{dx} = \frac{d(EC_g)}{dx} = -f_w \frac{\rho_I + \rho_{II}}{3\pi} \left(\frac{\sigma a}{\sinh kh_{II}}\right)^3 - \beta \frac{(\rho_I + \rho_{II})g}{4\pi\sqrt{2}} \sigma a^2 \tag{25}$$

where F = energy flux per unit of width; E = depth-integrated, time-averaged wave energy per unit area; f_w = friction coefficient; and β = energy dissipation coefficient.

3. Experiments

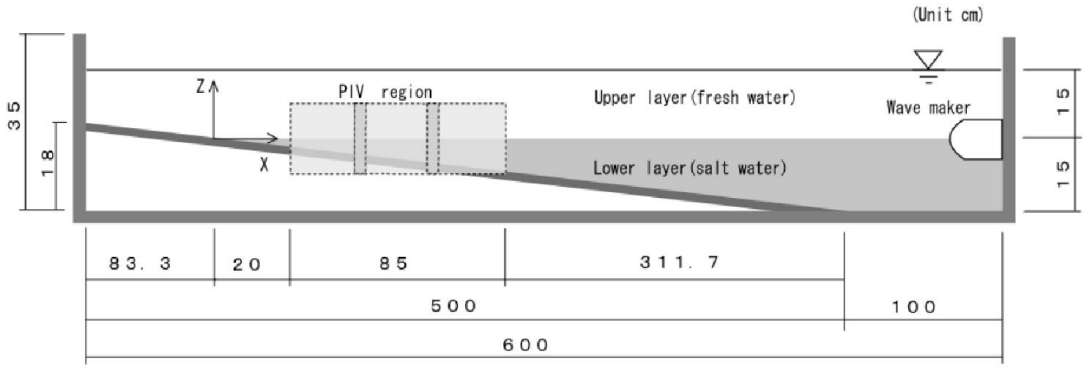

Figure 1. Sketch of apparatus

The experimental setup is represented schematically in Figure 1. The wave tank is 600cm long, 15cm wide, and 35cm deep. It is constructed of twelve Plexiglas panels, ten stainless flanges, and a stainless bottom. Each glass panel is 92cm long and 27cm high. A 1-cm-thick Plexiglas plate with a slope of 0.036 was placed between 100 and 600cm from the wall on the wavemaker side. A density-stratified fluid consisting of fresh and salt water with a density of 1028mg/cm³ was prepared for the experiments. The water depth was 30cm, and the upper-layer thickness was 15cm. The wave periods used in the present experiment were T = 5.2s for tests with a horizontal flap-type wavemaker, and T = 5.0 and 6.0s for tests with a slide-type wavemaker.

A flow visualization and video recording technique was used to quantify the displacement of the density interface. The salt water was dyed blue and the fresh water remained clear. Three video cameras (SONY DCR-TRV900) were placed at a distance of 2m from the wave tank.

These video cameras aimed at a front glass panel, and the video images were digitally recorded on DV tapes at 30 fps (frame per second). The field of view of each digital video camera was set to 40cm×25cm, and these fields overlapped by approximately 50%. The maximum resolution of the color images was 600×480 pixels, and the color depth of files was 8 bits. Each color image file was transferred to an 8-bit (256 grades) grayscale image file. Using the method of image segmentation, individual pixels in a grayscale image were marked as object or background pixels. The image was segmented into object and background pixels. The density interface was estimated from the spatial distribution of the threshold. The processed data were saved to ASCII files and transformed to real scale. Finally, the temporal displacements of the density interface were obtained at several points,

and the wave height and mean level were estimated by averaging these displacements over 10 wave periods.

The instantaneous water particle velocity induced by internal waves was measured using PIV. The basic principle of PIV is evaluating the instantaneous velocities through recording the position of images of small tracers, suspended in the fluid, at successive instants in time. In practice, when two successive images of tracers illuminated in a thin and intense light sheet are acquired, the velocity will be calculated from the known time difference and measured displacement. Our new PIV system utilizes halogen lamps and three high-definition digital video cameras (SONY HDR-SR1) in which the maximum resolution was 2016×1134 pixels and the images were recorded on a hard disk. Each video camera, operating simultaneously side by side, covered an area up to 40cm×22.5cm (frame rate 16:9). The field of view of video camera overlapped by 50%. Since the water surface was almost flat during all experiments, the halogen lamps were set in a line along the wave tank at its top, and the light sheet of 3mm width was emitted from the upper side of the wave tank. To capture the high-contrast images with the particle tracer in both layers, we used DIAION that consisted of ion-exchange resin with the homogeneous matrix structure inside the particle. The grain size and specific gravity were 2mm and 1.02, respectively.

4. Results

Figure 2 shows the spatial displacements of the density interface for a wave period of T = 5.2s at six different times. The abscissa is the distance from the intersection between the sloping bed and stationary level of the density interface, and the ordinate is the elevation above that level. The solid curve shows the theoretical solution based on the method of characteristics. The circular symbols show the position of the density interface by using the image processing technique.

Inspecting the six figures reveals that the method of characteristics predicts the measured profiles with a reasonable degree of accuracy in the range of the test condition. The absolute value of the crest level is larger than that of the trough level, and this tendency is prominent in the upper-slope region. Figure 3 depicts the corresponding variation of celerity in the near-shore region. The measured distribution of celerity is also plotted to compare with the theoretical celerity profiles given by the linear theory and by the method of characteristics. The measured celerity is smaller than predicted by the linear theory. On the other hand, the solution by the method of characteristics agrees well with the measured data of celerity. Comparisons of predicted and observed wave-height variations are presented in Figure 4 in which the setup of internal waves is also shown. In order to calculate the wave-height distribution, the value of β in Eq.(25) was determined using a trial-and-error procedure. In the present calculation, it was fixed and equal to 0.0035. Consequently, both computed wave-height attenuation and setdown qualitatively agree with the observed data.

Figure 5 represents a series of temporal displacements of the density interface for a wave period of T = 5.0s using a slide-type wavemaker at six horizontal locations along the wave tank.

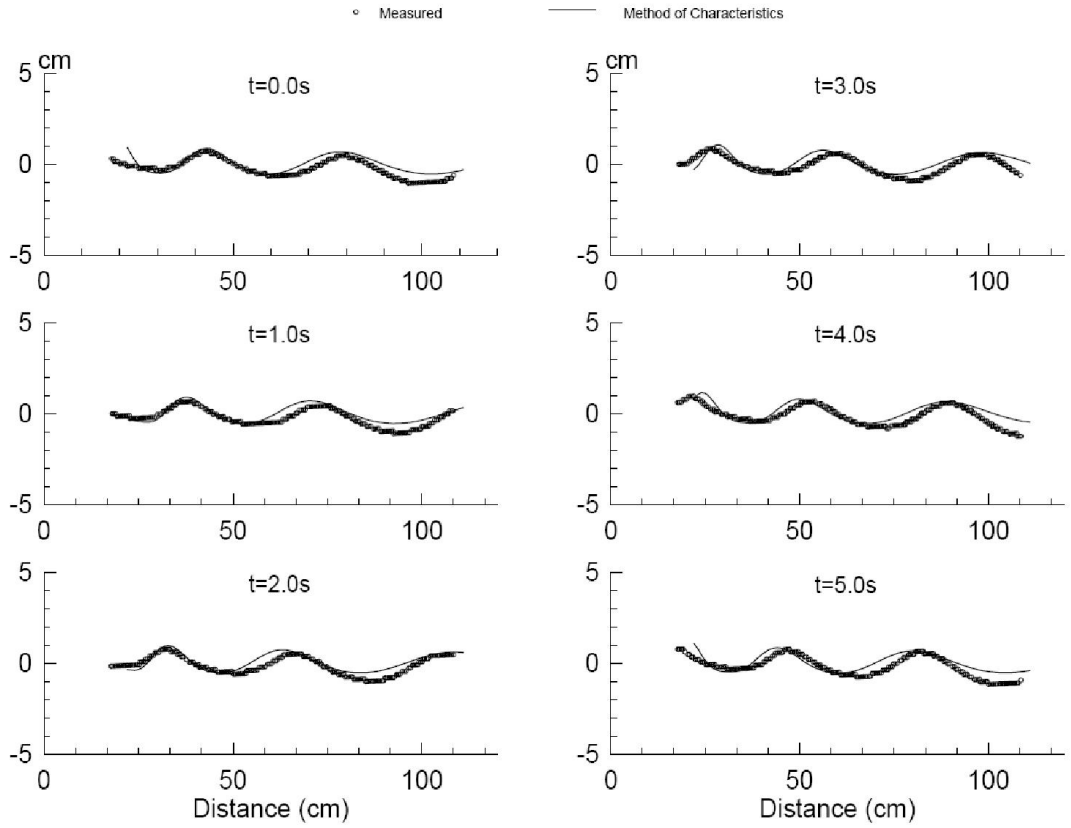

Figure 2. Spatial variations of density interface for $T = 5.2$s

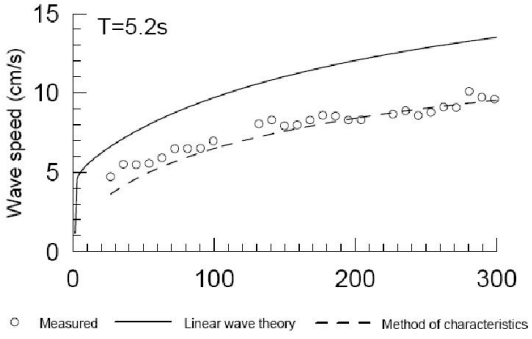

Figure 3. Measured and calculated profiles of celerity

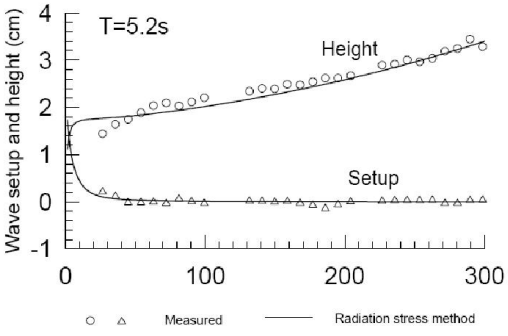

Figure 4. Attenuation and setup of internal waves

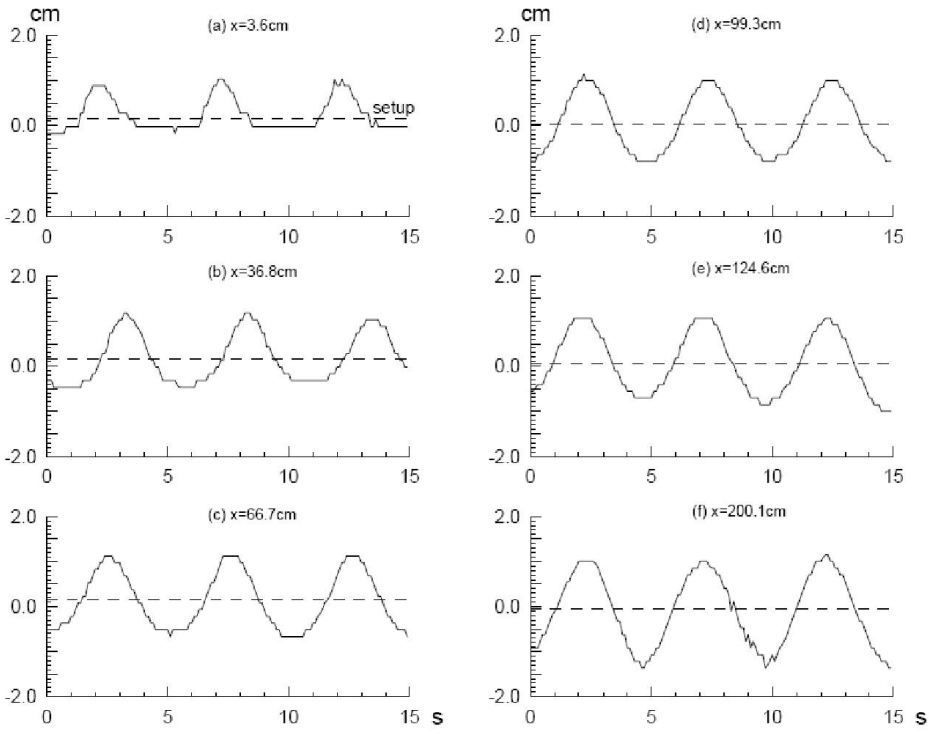

Figure 5. Temporal displacements of density interface for $T = 5.0$s

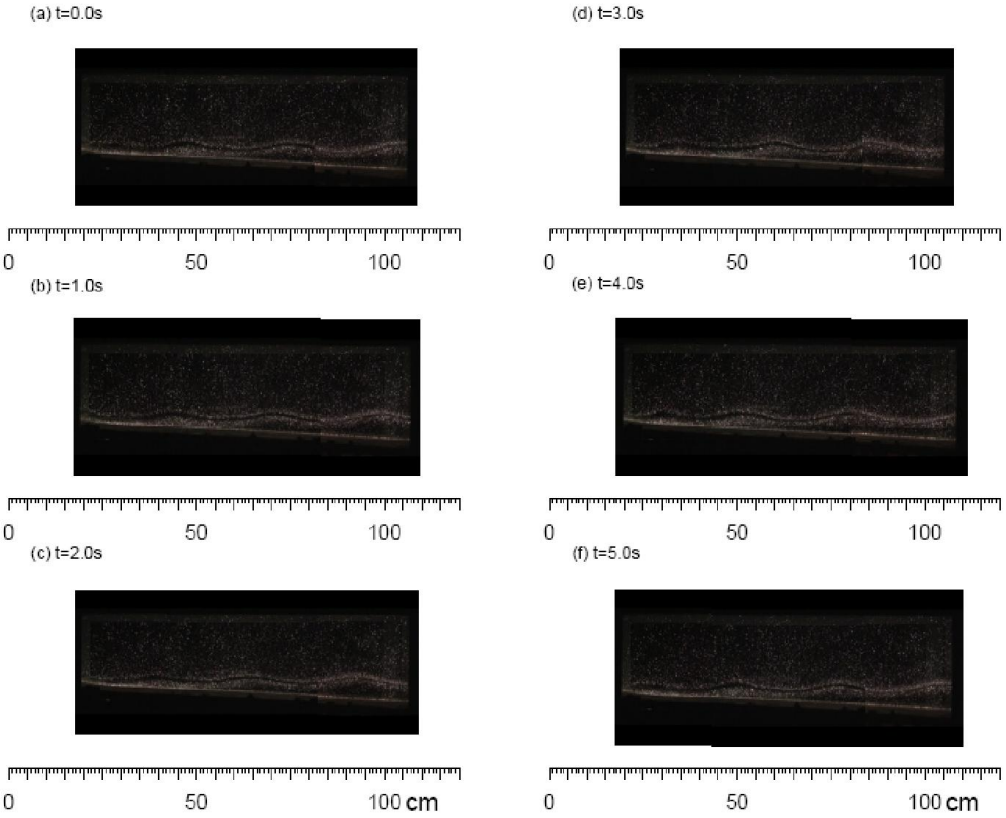

Figure 6 Video images of PIV experiment for $T = 5.0$s.

All waveforms differ considerably from a sinusoidal profile, but the general characteristics at any given location are quite similar. The internal waves show strong nonlinearity when propagating up the slope. Moving closer to the origin (x = 0), a prominent feature of the cnoidal-type fluctuations continues from one wave to the next. The wave height abruptly decreases, while its mean density interface slowly increases. The local mean level $\overline{\eta}$ averaged over 10 wave periods is also shown in each figure. These interfacial displacements exhibit a higher rise at the crest and a depression near the trough as the location approaches the origin. Figure 6 illustrates the shoaling of internal waves with a PIV experiment where the waves were generated with an oscillatory motion of T = 5.0s. Although the density gradient tends to cause the accumulation of DIAION near the density interface, plenty of particles are distributed in both layers. When internal waves are generated, the accumulation shows roughly the distortion of the isopycnals. A white boundary curve may represent the shape of an internal wave group. Each image consists of three pictures simultaneously taken by three video cameras. Waves are propagating from right to left in the upslope direction. These phases are T = 0.0, 1.0, 2.0, 3.0, 4.0, and 5.0s. The corresponding velocity fields at these phases are shown in Figure 7, indicating that an array of asymmetric vortices forms along the wave tank and their scale decreases as waves progress into the shallow-water region. The thinner clockwise vortex alternates with the thicker counterclockwise vortex. From a pair of counterrotating vortices, one can estimate the wave train. Each vortex has a quasi-elliptic form with its center located near the density interface.

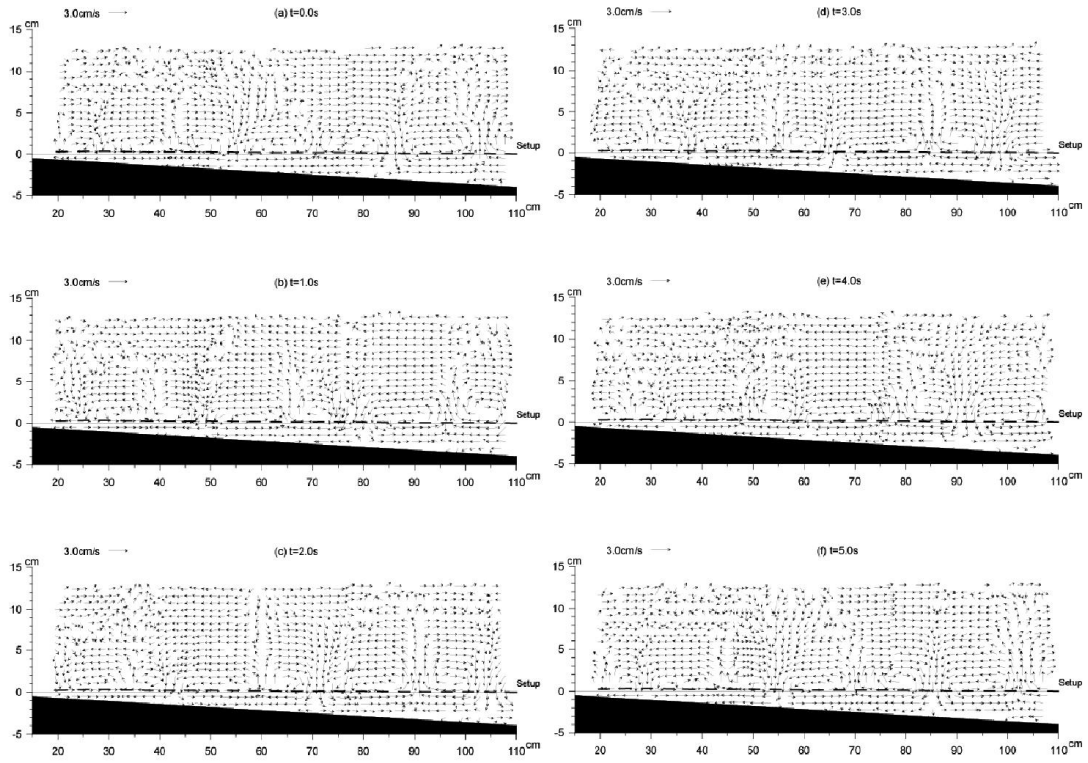

Figure 7. Instantaneous velocity fields for T = 5.0s

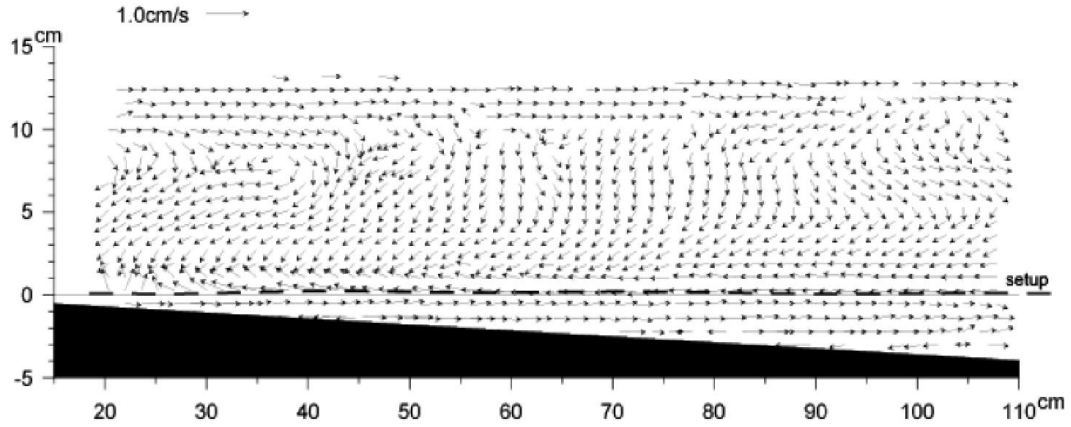

Figure 8. Mean velocity fields for T = 5.0s

Generally, the magnitude of velocity vector in the lower layer is larger than that in the upper layer. The flow under the density interface converges in the front of the wave crest, and diverges behind it. This contributes to creating trajectory systems in the upper and lower layers, without crossing the density interface. The velocity in a vortex reaches its maximum near the density interface. The vortex reaches its minimum size but does not disappear near the origin.

The formation of the bolus occurs one after another. Figure 8 illustrates the mean velocity field for T = 6.0s. The velocity vector was obtained by averaging both horizontal and vertical components of the instantaneous velocity over 10 wave periods and superimposing them. It is obvious that there is a strong mean flow up the shore close to the density interface in the upper layer and a return flow down in the lower layer. In the mid upper-layer region, the mean velocity directs downward because of the gravity effect.

5. Conclusions

In the present study, an image processing technique was used to quantify the spatial and temporal displacements of the density interface, and a PIV system with Halogen lamps was examined to illustrate the velocity fields in layers of fresh and salt water over a slowly varying water depth. The wave generation was made by a flap-type or slide-type wavemaker. Wave celerity, attenuation and setup of internal waves were investigated theoretically and experimentally. The energy dissipation model was used to predict the local wave height. The setup simulated with the momentum balance equation based on a radiation stress concept agrees with the measured setup. The instantaneous velocity fields by the PIV measurement showed that the thinner clockwise vortex alternates with the thicker vortex with an opposite rotational direction. The mean velocity fields revealed four distinct flow regions existing from the water surface to the sloping bottom.

References

[1] Longuet-Higgins, M.S., and Stewart, R.W. (1964). "Radiation stress in water waves; a physical discussion, with applications." Deep-Sea Res., 11, 529-562.

[2] Umeyama, M. (1998). "Second-order internal wave theory by a perturbation method." Memoirs, Tokyo Metropolitan University, Tokyo, 48, 137-145.

[3] Umeyama, M. (2002). "Experimental and theoretical analyses of internal waves of finite amplitude." J. Waterway, Port, Coastal, and Ocean Eng., 128(3), 133-141.

[4] Umeyama, M. (2008). "PIV techniques for velocity fields of internal waves over a slowly varying bottom topography." J. Waterway, Port, Coastal, and Ocean Eng., 134(5), 286-298.

[5] Umeyama, M., and Shintani, T. (2004). "Visualization analysis of runup and mixing of internal waves on an upper slope." J. Waterway, Port, Coastal, and Ocean Eng., 130(2), 89-97.

[6] Umeyama, M., and Shintani, T. (2006). "Transformation, attenuation, setup and undertow of internal waves on a gentle slope." J. Waterway, Port, Coastal, and Ocean Eng., 132(6), 477-486.

Biography

Prof. Dr. Motohiko Umeyama is the Professor of Coastal and Ocean Engineering at the Department of Civil and Environmental Engineering, Tokyo Metropolitan University (TMU). He received his Ph.D. degree in Ocean Engineering from University of Hawaii at Manoa. He was a research fellow at Delft University of Technology. He has also served as a consultant for several coastal protection and defense projects in Indonesia and the Cook Islands. His research interests include nonlinear wave theories, internal waves, and turbulent structure in wave and current field.